Structural and spectroscopic properties of the polar antiferromagnet Ni_{2}MnTeO_{6}

Maria Retuerto, Stella Skiadopoulou, Fedir Borodavka, Christelle Kadlec, Filip Kadlec, Jan Prokleška, Zheng Deng, Jose A. Alonso, Maria T. Fernandez-Diaz, Felix O. Saouma, Joon I. Jang, Dominik Legut, Stanislav Kamba, and Martha Greenblatt

Phys. Rev. B **97**, 144418 — Published 23 April 2018

DOI: 10.1103/PhysRevB.97.144418

Structural and spectroscopic properties of the new polar antiferromagnet Ni_2MnTeO_6

Maria Retuerto,[1] Stella Skiadopoulou,[2,3] Fedir Borodavka,[2] Christelle Kadlec,[2] Filip Kadlec,[2] Jan Prokleška,[4] Zheng Deng,[1] Jose A. Alonso,[5] Maria T. Fernandez-Diaz,[6] Felix O. Saouma,[7] Joon I. Jang,[8] Dominik Legut,[3] Stanislav Kamba,[2] and Martha Greenblatt[1*]

[1]*Department of Chemistry and Chemical Biology, Rutgers, The State University of New Jersey, 610 Taylor Road, Piscataway, NJ 08854, USA*

[2]*Institute of Physics,Czech Academy of Sciences, Na Slovance 2, 18221 Prague 8, Czech Republic*

[3]*IT4Innovations Center, VSB Technical University Ostrava, 17. listopadu 15, CZ-708 33 Ostrava-Poruba, Czech Republic*

[4]*Department of Condensed Matter Physics, Faculty of Mathematics and Physics, Charles University, Ke Karlovu 5, 121 16 Prague 2, Czech Republic*

[5]*Instituto de Ciencia de Materiales de Madrid, C.S.I.C., Cantoblanco, E-28049 Madrid, España.*

[6]*Institut Laue Langevin, BP 156X, Grenoble, F-38042, France*

[7]*Department of Physics, Applied Physics and Astronomy, Binghamton University, P.O. Box 6000, Binghamton, NY 13902, USA*

[8]*Department of Physics, Sogang University, 35 Baekbeom-ro, Mapo-gu, Seoul 04107, South Korea*

We present a structural and spectroscopic study of a new compound Ni_2MnTeO_6, closely related to the polar antiferromagnet Ni_3TeO_6 known to show a colossal magnetoelectric effect and pronounced elementary magnetoelectric excitations. For the first time, we prepared single crystals and polycrystalline samples of Ni_2MnTeO_6 showing the same polar structure as Ni_3TeO_6 from room temperature down to 4 K with the R3 space group symmetry. Magnetic and dielectric measurements have indicated an antiferromagnetic phase transition at $T_N \approx 70$ K, almost 20 K higher than that of Ni_3TeO_6. Extensive infrared, Raman and THz spectroscopy experiments were employed for investigating lattice and spin excitations, revealing all phonons predicted by the factor group analysis. THz spectra below T_N reveal one new excitation, which is strongly influenced by external magnetic field, thus assigned to a magnon.

In pursuit of multiferroic compounds with crystal structure other than that of the perovskites, the corundum-related (Al_2O_3) family $A_2BB'O_6$ scores a success among the magnetic systems,[1–11] and lately, due to the colossal magnetoelectric effect in the polar antiferromagnet Ni_3TeO_6, the multiferroic community.[12–16] In the above structural formula, A is usually a small diamagnetic, or paramagnetic divalent cation, B a divalent or trivalent transition metal cation, and B' a pentavalent or hexavalent transition metal or a diamagnetic cation (e.g., Sb, Te).

During the 80s, a few studies on corundum- and cryolite-related (a-Na_3AlF_6) compounds suggested ferroelectric (FE) properties for a series of M_3TeO_6 compounds, with M corresponding to paramagnetic cations, and the reported Curie temperatures around 500 K.[1,2] However, no evidence of non-centrosymmetric structure for any of the above compounds at room temperature was reported ever since, except for Ni_3TeO_6. Thus, Mg_3TeO_6[17] and Mn_3TeO_6[6] crystallize in the rhombohedral $R\bar{3}$ space group, Cd_3TeO_6[18] and Ca_3TeO_6[19] in the monoclinic $P2_1/n$, Co_3TeO_6 in the monoclinic $C2/c$,[20] and Cu_3TeO_6 in the cubic $I\alpha\bar{3}$[21] space groups. To date, Ni_3TeO_6 and $(Mn_{0.2}Ni_{0.8})_3TeO_6$ are the only reported compounds without inversion symmetry.[8] The $Ni_{3-x}Mn_xTeO_6$ system shows the $R3$ space group at room temperature, and, interestingly, it displays an antiferromagnetic (AFM) transition temperature of T_N=67 K,[8] higher than that in Ni_3TeO_6. A further increase in T_N upon increasing x was suggested by Mathieu *et al*.[8] in view of an expected stabilization of the $R3$ space group.

Aiming at enhancing the critical temperature, Ni_2MnTeO_6 was synthesized, for the first time, in the form of single crystals and ceramics; their magnetic and dielectric properties were studied, together with lattice and spin dynamics. Since Ni_3TeO_6 exhibits a strong magnetoelectric coupling which activates electromagnons in THz and Raman spectra,[15] we wanted to check for the presence of such spin excitations also in Ni_2MnTeO_6. The increase in T_N predicted by Mathieu *et al*.[8] was confirmed, since Ni_2MnTeO_6 exhibits an AFM transition at $T_N \sim 70$ K. In addition, the THz spectra unveil a spin excitation below T_N.

I. Experimental details

Polycrystalline Ni_2MnTeO_6 was prepared from stoichiometric amounts of analytical grade NiO, TeO_2 and $MnCO_3$. The mixture was heated in a tubular furnace under oxygen flux at 800ºC with intermediate grindings between 700 and 800ºC. Single crystals were prepared by the flux method in the following steps: Ni_2MnTeO_6: V_2O_5: TeO_2: NaCl: KCl in a molar ratio of 1:5:10:10:5 was kept for two days at 800ºC and then cooled down to 600ºC during three days. Plate-shaped green crystals with lateral dimensions of less than 1 mm were obtained. The structure and purity of the polycrystalline powders were determined by powder X-ray diffraction (XRD) (Cu K_{α}, λ = 1.5406 Å) and energy dispersive spectroscopy (EDS, X-ray microanalyzer JXA-733 Superprobe). For structural refinements, powder neutron diffraction (PND) was performed. PND was collected at the Institute Laue-Langevin, Grenoble. The data at room temperature were collected in the D2B High Resolution instrument (λ = 1.5940 Å). For the determination of the magnetic structure between 5 and 100 K we used the D20 (λ = 2.410 Å) instrument. Diffraction data analysis by Rietveld refinement[22] was performed with the Fullprof software[23] The structure of the single crystals was determined by single-crystal X-ray data collected on a Bruker Smart APEX CCD diffractometer with graphite-monochromatized Mo K_{α} radiation (λ = 0.71073Å) at 100 K. Magnetic measurements of the single crystals were performed on a Quantum Design SQUID system, whereas those of polycrystalline samples utilized the ACMS and VSM options (extraction and vibrating sample magnetometers) of the PPMS apparatus (Quantum Design) in fields up to 14 T and temperatures down to 2 K.

Near-normal incidence IR reflectivity spectra of the Ni_2MnTeO_6 ceramics were measured by a Fourier-transform IR spectrometer Bruker IFS 113v in the frequency range of 20-3000 cm^{-1} (0.6 – 90 THz) at room temperature; for the low-temperature measurements, an Optistat optical cryostat (Oxford Instruments) with polyethylene windows was used; their transparence reduced the spectral range to 20-650 cm^{-1}. A pyroelectric deuterated triglycine sulfate detector was used for the room-temperature measurements, whereas a He-cooled (T=1.6 K) Si bolometer was used for the low-temperature measurements down to 7 K.

THz measurements from 3 to 60 cm^{-1} (0.09 – 1.8 THz) were performed in the transmission geometry with a custom-made time-domain terahertz spectrometer. Here, a femtosecond Ti:sapphire laser oscillator (Coherent, Mira) produces a train of femtosecond pulses, which generate linearly polarized broadband THz pulses radiated by a photoconducting switch TeraSED (Giga-Optics). A gated detection scheme based on electrooptic sampling with a 1 mm thick [110] ZnTe crystal as a sensor allows one to measure the time profile of the electric field of the transmitted THz pulse. An Oxford Instruments Optistat optical cryostat with mylar windows was used for low-temperature measurements. THz experiments in an external magnetic field $H_{ext} \leq 7$ T were performed with an Oxford Instruments Spectromag cryostat in the Voigt configuration, where the electric component of the THz radiation $\boldsymbol{E}_{THz}$ was set parallel and perpendicular to $\boldsymbol{H}_{ext}$.

The IR reflectivity and THz complex permittivity spectra were fitted assuming a sum of N independent damped harmonic oscillators, expressed as:[24]

$$\varepsilon^*(\omega) = \varepsilon_\infty + \sum_{j=1}^{N} \frac{\Delta\varepsilon_j \omega_{TOj}^2}{\omega_{TOj}^2 - \omega^2 + i\omega\gamma_{TOj}} \qquad (1)$$

where $\Delta\varepsilon_j$ is the dielectric strength of the j-th mode, ω_{TOj} the frequencies of the j-th transverse optical (TO) phonons, and γ_{TOj} are the corresponding damping constants. ε_∞ is the high-frequency (electronic) contribution to the permittivity, determined from the room-temperature frequency-independent reflectivity tail above the phonon frequencies. The reflectivity R(ω) is related to the complex dielectric function ε*(ω) by:

$$\boldsymbol{R}(\omega) = \left| \frac{\sqrt{\varepsilon^*} - 1}{\sqrt{\varepsilon^*} + 1} \right|^2 \qquad (2)$$

For Raman studies of single crystals, a Renishaw RM 1000 Micro-Raman spectrometer with Bragg filters was used, equipped with an Oxford Instruments Microstat continuous-flow optical He cryostat. The experiments were performed in the backscattering geometry in the 5–1800 cm^{-1} range. An Ar^{+}-ion laser operating at 514.5 nm was used. The spectra were carefully fitted with a sum of independent damped harmonic oscillators multiplied by the corresponding Stokes temperature factor.[25]

Spin-polarized density functional theory calculations were conducted, implementing the projector-augmented-wave formalism to describe the electron-ion interactions, and the generalized gradient approximation parametrized by Pedrew, Burke, and Ernzerhof (GGA-PBE) for the exchange-correlation potential.[26,27] To account for the correct AFM order, the unit cell was doubled along *c*-axis and sampled by 5x5x2 grid. The lattice dynamics calculations were used within the Phonopy code, employing calculated Hellman Feynman forces, and using 2x2x2 supercell with 60 displacements of 0.01 Å. Additional on-site Coulomb repulsion interactions were considered concurrently, within the rotationally invariant form of the GGA+U approach,[28] where the localized 3*d* electrons experience a spin- and orbital-dependent potential (*U*) and the exchange interaction *J*, while the other orbitals are delocalized and treated by the conventional GGA approximation.

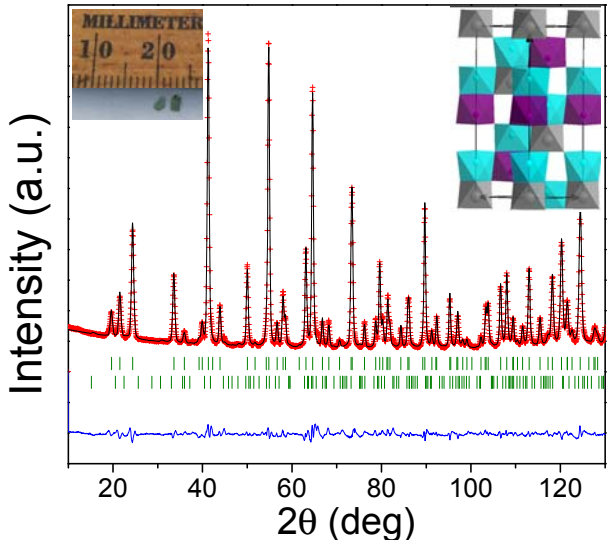

Figure 1 PND pattern of Ni_2MnTeO_6. The lower row of Bragg reflections (green lines) represents an impurity of Mn_3TeO_6 amounting to 3%. Left inset: photograph of the Ni_2MnTeO_6 single crystals. Right inset: schematic representation of the crystal structure, cyan: NiO_6 octahedra, purple: MnO_6 octahedra, and grey: TeO_6 octahedra. The displacements of the atoms from the octahedral center can be seen.

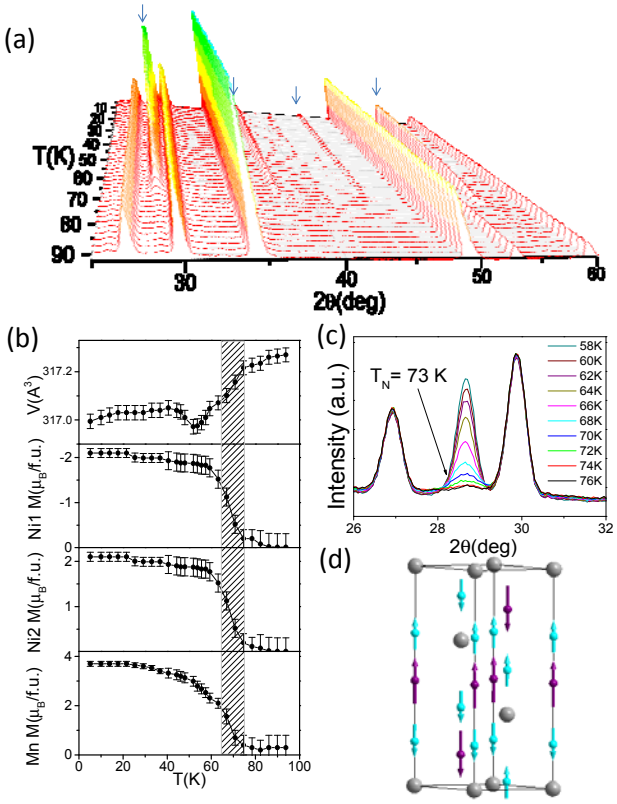

Figure 2 (a) Thermal evolution of the PND pattern of polycrystalline Ni_2MnTeO_6, showing the peaks related to the AFM transition at ~70 K. (b) Temperature dependence of the unit cell volume and magnetic moments per magnetic cation. (c) Prominent magnetic transition at 73 K, as seen by the evolution of the PND peak. (d) Schematic representation of the AFM configuration (the magnetic unit cell is larger) (purple: Mn, cyan: Ni).

II. Results and discussion

A. Structural Characterization

Based on the room-temperature PND (Figure 1) and XRD characterization, we determined that the structure of Ni_2MnTeO_6 is analogous to that of Ni_3TeO_6 (rhombohedral, space group *R*3 (No. 146), Z = 3), which can be viewed as a $A_2BB'O_6$-type corundum derivative. The structure contains two crystallographically distinct Ni atoms at the A-sites, denoted here as Ni^{I} and Ni^{II}, ordered Mn and Te on both B sites, and two independent oxygen atoms (for details see Tables S1 and S2 in Supplemental Information).[29] XRD on single crystals revealed slightly different lattice parameters, which can be explained by a small difference between Ni/Mn ratios in crystals and ceramics. The structure is formed by layers of edge-sharing TeO_6 and $Ni^{I}O_6$ octahedra in the *ab* plane; these layers alternate with those containing edge-sharing MnO_6 and $Ni^{II}O_6$ octahedra. The layers are connected along the *c* axis by face-

sharing dimers of $TeO_6/Ni^{II}O_6$ and $MnO_6/Ni^{I}O_6$ (see Inset of Figure 1). The non-centrosymmetricity of Ni_2MnTeO_6 structure was supported by SHG measurements (Supplemental Information, Figure S2).[29]

Due to electrostatic repulsion, the cations inside the face-sharing octahedra are displaced from their centers along the *c* direction, moving closer to the octahedral vacancies and farther away from the other cation in the dimer. This gives rise to three long and three short octahedral separations. This effect is more pronounced in Ni_2MnTeO_6 than in Ni_3TeO_6,[30] and it is analogous to that in the isostructural Mn_2FeWO_6.[16]

B. Magnetic Structure

In order to determine the magnetic structure, PND at low temperatures was measured. The temperature dependences of the diffraction pattern, unit cell volume and magnetic moments are shown in Figure 2(a), (b). The magnetic transition is clearly observed at $T_N \approx 70$ K (Figure 2(c)), nearly 20 K higher than in Ni_3TeO_6. The magnetic structure (Figure 2(d)) is AFM, characterized by a propagation vector **k**= (0 0 3/2), and it consists of spins ferromagnetically ordered in adjacent *ab*-planes, pairwise alternately pointing parallel and antiparallel along the *c* direction.

The magnetic moments at Ni^{I}, Ni^{II} and Mn sites at 5 K were refined as 2.1(2) μ_B/f.u. for Ni and 3.7(3) μ_B/f.u. for Mn. The moments at the Ni positions are slightly larger than those expected for the Ni^{2+} spin state S=1, which can be explained by the disorder with Mn^{2+}, expected to exhibit a spin state of S=5/2. And the same with Mn moments, that are slightly smaller than expected due to the partial disorder.

Employing first-principles calculations, we have determined the structural geometry with the AFM order as depicted in Figure 2(d). The calculated hexagonal lattice parameters of a= 5.21386 Å and c=14.17241 Å, correspond to a less than 1% higher volume value than the experimental one (see Table S1 in Supplemental Information).[29] Within the GGA+U approach, the $U_{eff}=U-J$ is only meaningful, where $U_{eff}=7$ eV for both Ni and Mn sites, yield the Ni and Mn magnetic moments: 1.8 μ_B and 4.8 μ_B, respectively. These values lie close to the previously reported experimental ones for Ni (2 μ_B) and Mn (3-6 μ_B), in the Ni_3TeO_6[31] and Mn_3TeO_6[32] compounds, respectively.

C. Magnetic and dielectric properties

The temperature dependence of the magnetic susceptibility measurements for Ni_2MnTeO_6 single crystal is displayed in Figure 3(a), for two orientations of the magnetic field: $\boldsymbol{H}_{ext} \parallel c$ and $\boldsymbol{H}_{ext} \perp c$. The AFM transition occurs at ca. 67 K, and it is markedly stronger in the susceptibility along *c*, as expected from the magnetic structure (Figure 2). The discrepancy between the values of the Néel temperature, 73 K from PND data and 67 K from the magnetic measurements, can be ascribed to the different experimental techniques, and to the use of different samples (polycrystalline in the former and single crystalline in the latter case) with slightly different Ni/Mn ratios. Figure 3(b) shows the temperature dependence of permittivity in the ceramics measured at 1 MHz. Since the magnetic structure was shown to be collinear with the *c* axis, the decrease in χ observed below T_N for $\boldsymbol{H}_{ext} \perp c$ is probably an artifact of a partial sample misalignment. The dielectric anomaly appearing at 67 K, at the AFM transition, indicates an interplay between the magnetic and polar characters (i.e. change in the electric polarization) of the phase transition. An additional dielectric anomaly is clearly seen at 23 K. This temperature corresponds to a phase transition in Mn_3TeO_6 which is AFM and probably FE.[6] The Mn_3TeO_6 secondary phase, amounting to ca. 3%, is observed by PND (Figure 1). According to literature, Mn_3TeO_6 should conserve the non-centrosymmetric rhombohedral $R\bar{3}$ space group down to 5 K.[6] However, Zhao *et al*.[33] reported a FE phase transition a few K below the AFM one, at around 21 K. The FE distortion is so small that it was not detected in previously published PND studies,[6] and Ivanov *et al*.[34] attempted to perform

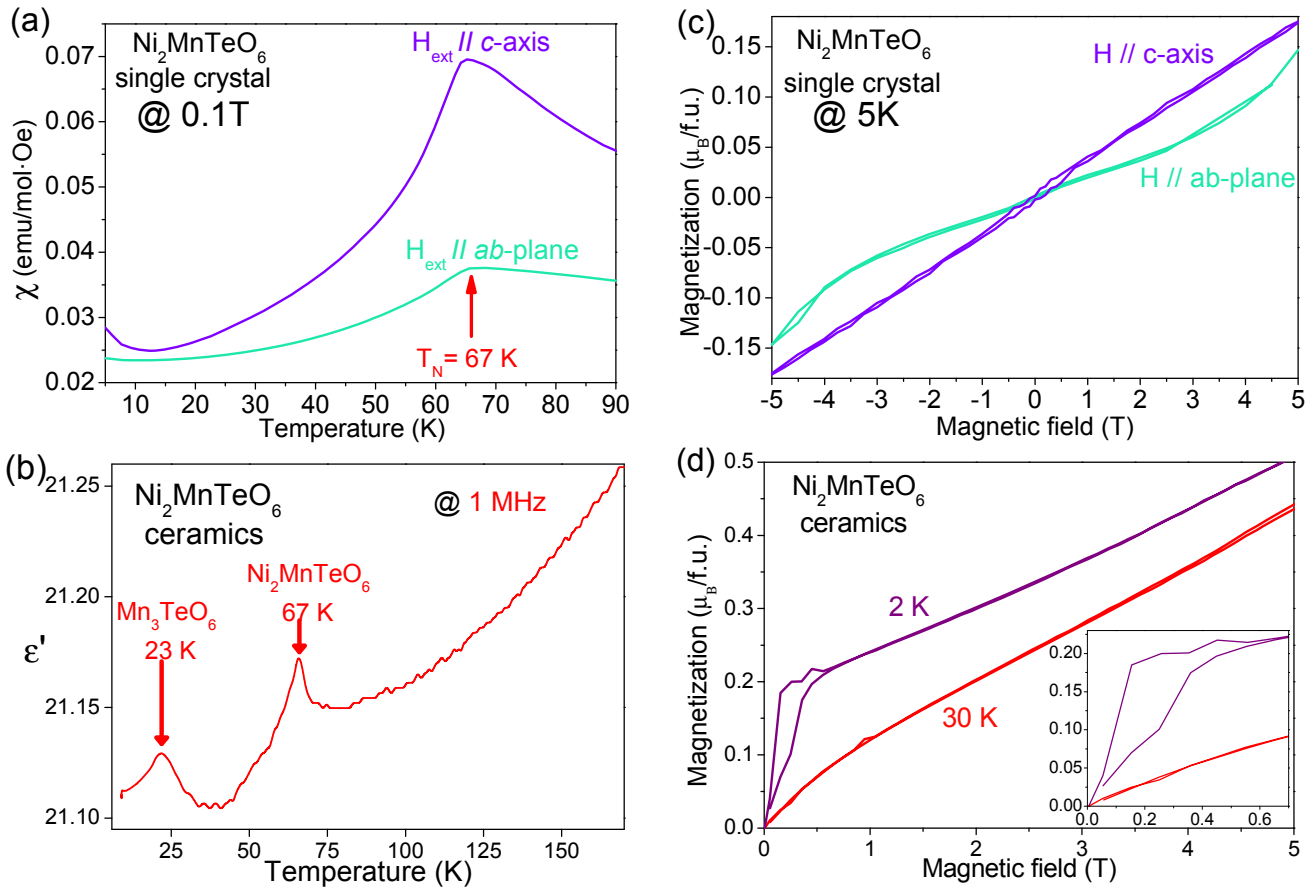

Figure 3 (a) Temperature dependence of magnetic susceptibility of the Ni_2MnTeO_6 single crystal at 0.1 T with two distinct orientations: $\boldsymbol{H}_{ext} \parallel c$ and $\boldsymbol{H}_{ext} \perp c$; the anomaly appears at ~67 K. (b) Temperature dependence of the permittivity of Ni_2MnTeO_6 ceramics, recorded at 1 MHz; the anomaly occurring around 67 K is due to the spin-order-induced FE transition, whereas the one anomaly at 23 K is probably due to a FE phase transition in the secondary phase of Mn_3TeO_6. (c), (d): magnetic–field dependences of magnetization in the single crystal and ceramics, respectively. In the single crystal, a spin-flop transition occurs at ~4.5 T, which is not observed in the ceramics. Inset of (d): low-magnetic-field hysteretic behavior in the ceramics, most probably due to the Mn_3TeO_6 secondary phase.

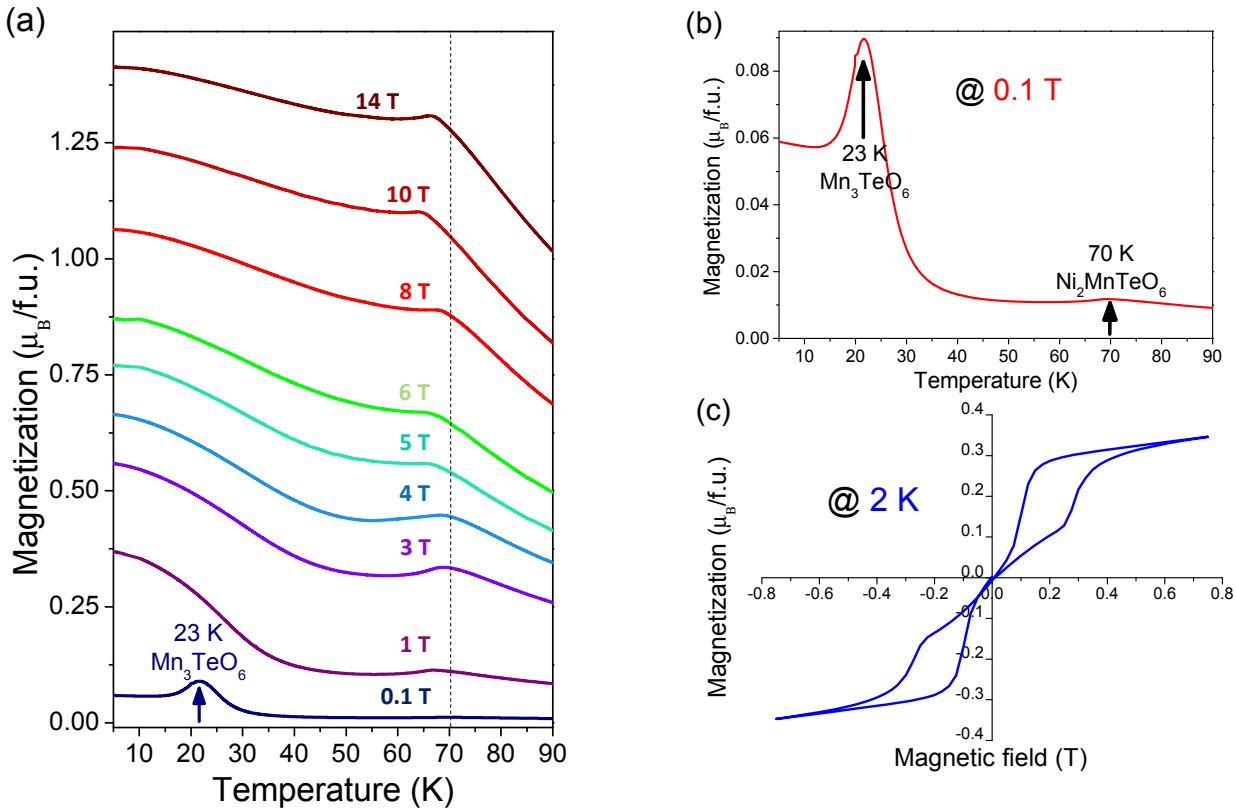

Figure 4 Temperature dependence of magnetization of Ni_2MnTeO_6 ceramics (a) up to 14 T, (b) at 0.1 T. Two conspicuous AFM transition temperatures of 23 and 70 K attest the presence of two distinct phases, Mn_3TeO_6 and Ni_2MnTeO_6, respectively. (c) A hysteretic magnetic-field dependence of magnetization of Ni_2MnTeO_6 ceramics, recorded at low magnetic fields of up to 0.8 T and at 2 K.

a more detailed structural analysis in order to explain this intriguing behavior, however, with no success. Note that for most of spin-order induced FEs, the FE distortions were not resolved in diffraction experiments, but only in dielectric measurements, because the FE distortions are usually very small.[35]

In Figure 3(c) and (d), the magnetic-field dependences of the magnetization for both the single crystal (c) and ceramics (d) are presented. The single-crystal experiment was done at 5 K and for two magnetic field orientations: $\boldsymbol{H}_{ext} \parallel c$-axis and $\boldsymbol{H}_{ext} \parallel ab$-plane, with $\mu_0 H$ of up to 5 T. The ceramic sample was measured at 2 and 30 K, up to 14 T, however here we present data only up to 5 T. The single crystal shows an easy-axis magnetization along *c,* and a non-hysteretic spin-flop transition around 4 T, resembling its unsubstituted counterpart Ni_3TeO_6, which manifests a non-hysteretic spin-flop transition at ~8 T.[12] Curiously, the ceramic sample only presents a very weak bend in the magnetization curve at ~4.5 T, whereas a hysteretic behavior, possibly of a FM origin, appears at very low fields, below 0.3 T (see inset of Figure 3 (d)). We attribute this hysteresis to the secondary Mn_3TeO_6 phase in the ceramics sample. The secondary phase is also responsible for the higher magnetization of ceramics than that of the crystal, because Mn_3TeO_6 has a susceptibility higher than Ni_2MnTeO_6.[6]

Figure 4(a) presents the temperature dependences of magnetization for the polycrystalline Ni_2MnTeO_6 at various values of applied magnetic field. For any value of H, the magnetic transition takes place at ~70 K, in agreement with the PND results.

A noteworthy anomaly at 23 K suggests another magnetic transition (Figure 4(b)). We observed this anomaly in the PND but not in the single crystal susceptibility measurements (Supplemental Information, Figure S3). As mentioned above, the magnetic transition at 23K corresponds to Mn_3TeO_6 in the polycrystalline sample. Another possible explanation for the 23 K feature might be linked to impurities from the grain boundaries, which can contribute to the total magnetization. The magnetic structure of Ni_2MnTeO_6 ceramics changes above 0.4 T (a double hysteresis loop is seen - Figure 4(c)), and therefore the low-temperature anomaly in M(T) (Figure 4(a)) disappears at higher fields.

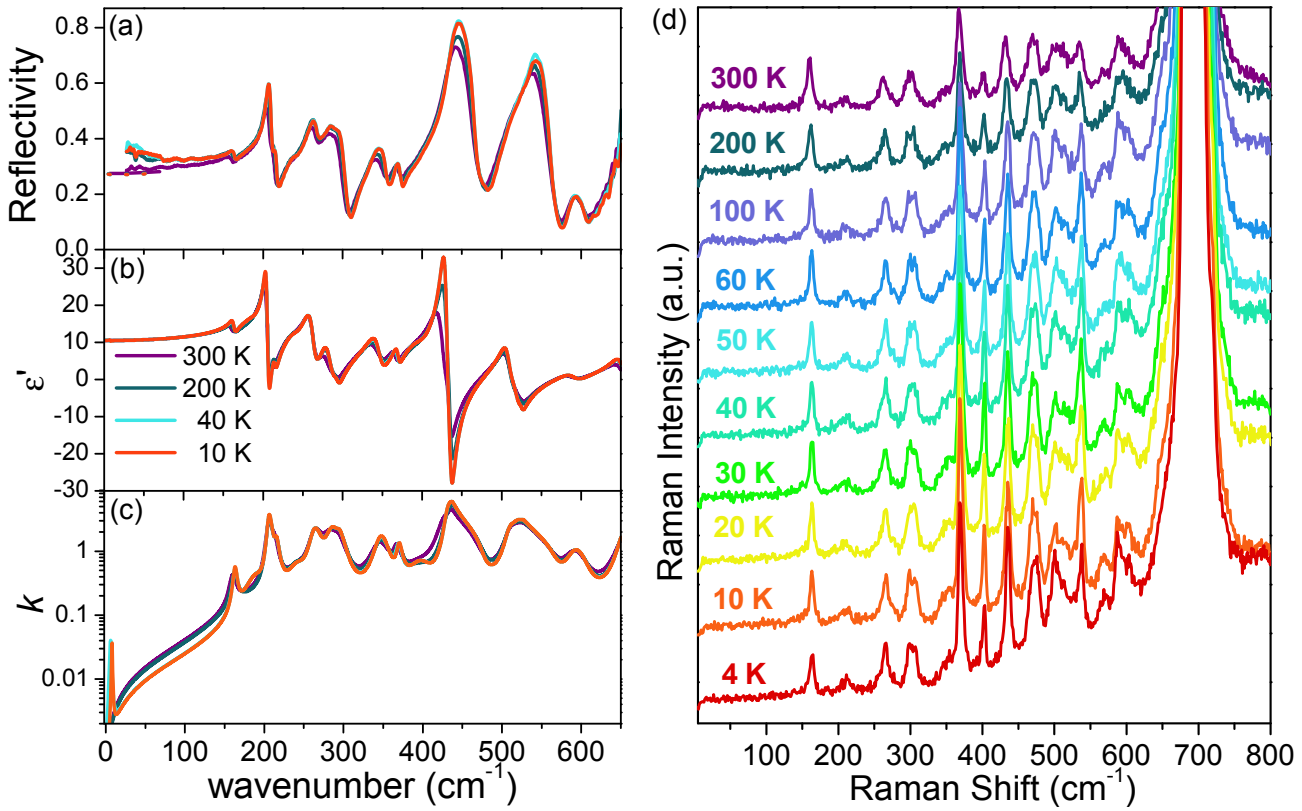

Figure 5 (a) IR reflectivity spectra measured at selected temperatures from 10 to 300 K. (b) Real part of permittivity and (c) imaginary part of index of refraction, as obtained from the fits or IR reflectivity and experimental THz spectra using Eqs. (1), (2). (d) Raman cross-polarized spectra for different temperatures from 4 to 300 K.

Since pure Ni_3TeO_6 exhibits a colossal static magnetoelectric coupling at the spin-flop transition near 8 T and a similar spin-flop transition occurs in Ni_2MnTeO_6 4 T lower, pyrocurrent and capacitance measurements of Ni_2MnTeO_6 crystals at external magnetic field are required. Unfortunately, the small size of our crystals did not allow such experiments. Growth of larger single crystals required for these experiments (more than 1 mm in diameter) is in progress.

D. Spin and lattice excitations

The IR reflectivity spectra of the Ni_2MnTeO_6 ceramics for selected temperatures from 10 to 300 K are shown in Figure 5(a), together with the fitted complex permittivity (Figure 5(b,c)). As predicted by the factor-group analysis for the *R*3 structure, nine $E(x,y,x^2\text{-}y^2,xy,xz,yz)$ and nine $A(x^2+y^2,z^2,z)$ modes are expected, both IR and Raman active, analogously to the Ni_3TeO_6 case.[15,36] All 18 modes are clearly visible in the IR spectra up to 300 K. Similarly to Ni_3TeO_6, the phonon eigenfrequencies are practically unaffected by temperature changes, since the *R*3 space group is preserved at all investigated temperatures. The damping of the modes slightly decreases upon cooling, as expected. A few of the mode frequencies lie close to the values of those reported for Ni_3TeO_6,[15,36] most of them corresponding to the vibrations of the TeO_6 octahedra.[37] The eigenfrequency values of the measured IR-active modes at 10 K, together with the respective damping and dielectric strength, are presented in Table 1. For comparison, the previously published Ni_3TeO_6 IR modes at 7 K by Skiadopoulou *et al.*[15] are also listed. The possible structural distortion at the AFM (and FE) transition at 67 K suggested by the anomaly in the permittivity data (Figure 3(b)) should have only a negligible effect on the IR spectra.

In Figure 5(b) and (c), permittivity ε'(ω) and extinction coefficient $k(\omega)$ spectra are displayed, respectively. Here we plot $k(\omega)$ spectra because we are not sure whether the excitation seen below 10 cm^{-1} contributes to permittivity or magnetic permeability. These spectra were extracted by fitting the IR reflectivity spectra of Figure 5(a) and complex THz spectra (Figure 6) by damped harmonic oscillators (Eqs. (1) and (2)). The static permittivity obtained from the fits amounts to ~10, close to the value of ~11 reported in the radio-frequency range for Ni_3TeO_6 by Oh *et al.*[12] The permittivity of our ceramics at 1 MHz (Figure 3(b)) even exceeds 20, but it is probably enhanced by a contribution of interlayer barriers

on grain boundaries, which are responsible for a Maxwell-Wagner contribution to the permittivity,[38] dominant especially above 100 K.

The highly dense ceramics allowed micro-Raman studies with the possibility of focusing at a single grain, since the laser spot diameter (~4 μm) was much smaller than the typical grain size of 30 μm (confirmed by Scanning Electron Microscopy micrographs – see Figure S1 in Supplemental Information)[29]. The spectra were collected in the back-scattering geometry, in both parallel and crossed polarizations, at temperatures from 4 to 300 K. Here, only the crossed polarized spectra are presented, since no significant differences between the two polarizations were observed, except for different intensity magnitudes. A plot of the Raman spectra at selected temperatures from 4 to 300 K is shown in Figure 5(d). The Raman mode frequencies at 4 K are presented in Table 1 in comparison with the IR modes at 10 K. The polycrystalline nature of the samples is not suitable for a symmetry analysis of the observed modes. All Raman modes which are not IR active correspond most probably to longitudinal optical modes (similarly as in Ni_3TeO_6 – see Ref. [15]). As for the IR spectra, no substantial changes were observed on cooling, apart from splitting of the mode at around 600 cm^{-1} and an expected decrease in damping. Such splitting originates mainly from the decrease in damping and a possible small frequency shift of the order of 1 cm^{-1}, due to thermal contraction. No new modes due to a possible change of crystal symmetry, or due to appearance of spin excitations, activate below T_N. This absence of newly-activated phonons in Raman and IR spectra below T_N supports the fact that the crystal symmetry is the same in the paramagnetic and ferromagnetic phases, belonging to the polar $R3$ space group.

Lattice dynamics calculations, based on the computed Hellman Feynman forces, yield all expected 18 IR- and Raman-active phonon modes. The computed values are in good agreement with the experimental ones obtained by IR and Raman spectroscopies (see Table 1).

Time-domain THz transmission measurements were performed for the Ni_2MnTeO_6 ceramics (thickness 1.9 mm), at temperatures from 4 to 300 K. Figure 6 shows the THz spectra for selected temperatures. Upon cooling, a gradual decrease in the real part of the index of refraction occurs. The increase in n with frequency comes from the phonon contribution, and the value of n~3.2 is in agreement with the static permittivity value obtained from the IR spectra. A new low-frequency excitation at ~ 6 cm^{-1} appears at 60 K, below the AFM transition of ~70 K, and upon cooling it sharpens and shifts to 8 cm^{-1} at 4 K. Note that the signal is rather noisy below 8 cm^{-1}, since it is close to the border of the accessible frequency region. The emergence of the new excitation below the magnetic transition, in combination with the fact that all 18 phonons predicted by the factor-group analysis are resolved in the IR and Raman spectra, suggest that this new excitation is of magnetic origin. The broader feature, also notable at higher frequencies (~40 cm^{-1}) in the $k(\omega)$ spectra, and equally emerging below T_N, is possibly due to multimagnon absorption. However, it may also correspond to a single-magnon excitation, since a similar feature at 32 cm^{-1} was observed in Ni_3TeO_6; the high value of damping could be attributed to the chemical disorder of Mn in the lattice (PND revealed Mn in B-sites of $A_2B_2O_6$ with an occupancy rate of 93%, whereas 7% of B-sites are occupied by Ni – see Table S1 in Supplemental Information).[29]

We measured THz spectra also in an external magnetic field of up to 7 T in the Voigt configuration, with $\boldsymbol{H}_{ext}$ parallel and perpendicular to the electric vector $\boldsymbol{E}^{\omega}$ of the THz beam. Here, we present only the spectra with $\boldsymbol{H}_{ext} \perp \boldsymbol{E}^{\omega}$ (Figure 7), where the magnetic-field effect upon the spin excitation was more pronounced (yet qualitatively the same). At 30 K (Figure 7(left)), the magnetic mode below 10 cm^{-1} shifts down and sharpens with increasing magnetic field. At 5 K (Figure 7(right)), a conspicuous sharpening up to 4 T takes place, followed by decrease in its intensity upon increasing $\boldsymbol{H}_{ext}$ up to 7 T.

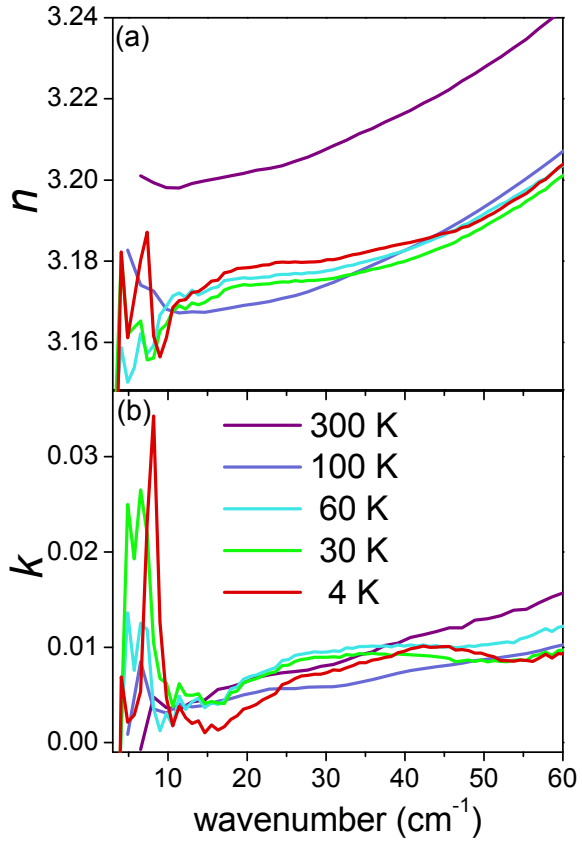

Figure 6 Temperature dependence of the (a) real and (b) imaginary part of the complex index of refraction, obtained from THz time-domain spectroscopy.

Table 1 Frequencies of the IR-active modes in the Ni_2MnTeO_6 ceramics at 10 K and Raman-active modes at 4 K, as obtained by fits of IR reflectivity with $\varepsilon_\infty = 3.9$. The low-frequency mode in the first line was identified in the THz spectra as a magnon. The first column corresponds to the IR mode frequencies of Ni_3TeO_6 ceramics at 7 K from Skiadopoulou *et al.*[15] The damping constants and dielectric strengths of the IR-active modes are also listed. The modes observed as weak in Raman spectra are marked by w in subscript. All Raman modes which are not IR active correspond to longitudinal optic modes. The theoretical frequencies obtained by first-principles calculations are also included, together with the assigned symmetry for each mode in the parentheses.

Ni_3TeO_6[15]	Ni_2MnTeO_6				
IR 7 K	Calculations	Raman 4 K	IR 10 K		
ω_{TO} (cm^{-1})	ω (cm^{-1})	ω (cm^{-1})	ω_{TO} (cm^{-1})	γ_{TO} (cm^{-1})	$\Delta\varepsilon$
16.2			7.9	1.3	0.04
32.4					
	168.0 (A)	164.6	163.1	5.8	0.12
185.0	195.4 (E)	185.5$_w$	189.2	28.5	0.34
	206.8 (A)	211.2	205.4	5.4	0.85
219.3	220.8 (E)		214.8	6.4	0.16
232.1	243.6 (A)		240.9	23.9	0.23
259.2	265.6 (E)	266.0	262.8	14.5	0.83
279.3	284.9 (E)		284.2	17.3	0.74
303.1	319.4 (E)	300.0	293.6	8.7	0.07
313.2	352.8 (A)	354.1$_w$	345.8	18.1	0.50
345.2	368.7 (E)	369.7	369.8	7.2	0.10
361.7	408.1 (A)	403.2	397.2	33.4	0.25
380.0	440.0 (A)		431.4	9.8	1.17
406.6	443.7 (A)	436.5	435.7	6.3	0.21
454.2	507.7 (E)	475.6	509.3	14.4	0.29

466.1		484.3			
516.5	546.8 (E)	501.6	518.7	17.1	0.31
536.6	555.3 (E)	538.0	525.5	5.5	0.01
		570.8_w			
597.1	587.1 (A)	590.6	590.6	24.6	0.09
661.2		603.4_w			
	663.4 (A)	681.0_w	653.9	17.7	0.27
		693.6			
		720.0_w			

Such behavior might be related to the spin-flop transition occurring at around 4.5 T (Figure 3(c)) or to the frequency limit of our experimental setup. Nevertheless, at 5 K a clear magnon frequency softening is exhibited with increasing $\boldsymbol{H}_{ext}$, from 8 cm^{-1} at 0 T to 6 cm^{-1} at 7 T.

Finally, the very small size of the single crystals did not allow for performing spectroscopic studies based on the orientation of the crystal structure. For example, directional dichroism might reveal the character of the spin excitation observed in the THz spectra and identify whether it corresponds to a pure magnon or electromagnon, as in Ni_3TeO_6. Unfortunately, since the magnetic excitation lies below 8 cm^{-1}, more precise transmission measurements with a spectrometer based on backward-wave oscillator sources[39] and a crystal with diameter at least 10 mm would be required. In addition, using single crystals, one can avoid possible impurities often present at grain boundaries of polycrystalline samples, thus the anomaly seen at 23 K could be absent or better resolved. Last but not least, capacitance and pyrocurrent measurements of Ni_2MnTeO_6 single crystals in external magnetic field could shed more light on the magnetoelectric properties of Ni_2MnTeO_6, since the very similar compound Ni_3TeO_6 presents a colossal magnetoelectric effect at the spin-flop transition occurring near 8 T.

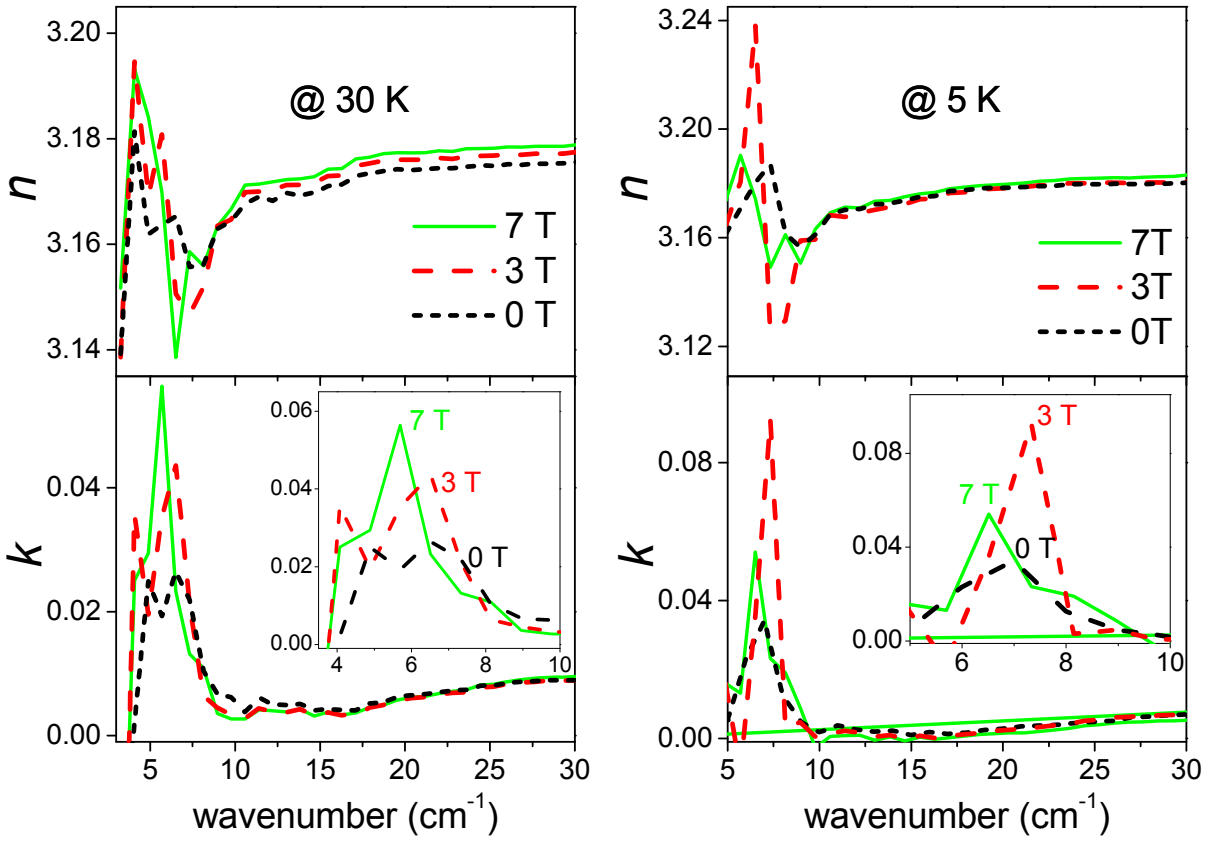

Figure 7 Real and imaginary part of index of refraction from the THz measurements of Ni_2MnTeO_6 ceramics, at external magnetic field in Voigt configuration $\boldsymbol{H}_{ext} \perp \boldsymbol{E}^{\omega}$, for 30 K (left) and 5 K (right) as measured.

III. Conclusions

Single crystals and polycrystalline ceramic samples of the new compound Ni_2MnTeO_6 were synthesized for the first time. The Mn-substitution of Ni in Ni_3TeO_6 leads to an increase in the AFM transition temperature by 20 K, thus reaching ~70 K, whereas the compound preserves the polar *R*3 space group. At the same time, an anomaly is also seen in the low-frequency permittivity spectrum. Another anomaly observed at 23 K is likely due to a Mn_3TeO_6 impurity phase. A spin-flop transition is triggered by an external magnetic field above 5 T, i.e. ~3 T lower than that of Ni_3TeO_6. Since in Ni_3TeO_6 a colossal magnetoelectric effect close to the spin-flop transition is known to exist, a strong static magnetoelectric coupling in Ni_2MnTeO_6 might appear at a lower magnetic field. To that aim growth of larger single crystals suitable for magnetoelectric studies is in progress.

The high-quality dense ceramic samples revealed all expected IR and Raman active modes of the *R*3 symmetry. A magnetic-field-tunable spin excitation at ~8 cm^{-1} is clearly seen in the THz spectra below T_N. Such a low frequency of the magnon does not allow for measuring also its Raman spectra, leaving the question open whether the magnon bears a magnetoelectric character. THz measurement of directional dichroism could reveal the character of the spin excitation (magnon or electromagnon). However, single crystals with more than 3 mm in diameter are required for such an experiment and these are not yet available.

Acknowledgements

The work of MG, MR and ZD was supported by the NSF-DMR-1507252 grant. MR also acknowledges the Juan de la Cierva program of the Spanish Ministry of Economy and Competitiveness for a grant FPDI-2013-17582. The work of SK, SS, FB, CK and FK was supported by European Union funding under the 7th Framework Programme (Project NOTEDEV), by the Czech Science Foundation (Projects 15-08389S and 18-09265S) and MŠMT KONTAKT II project LH15122. EDS characterization of ceramics performed by K. Jurek is highly appreciated. JAA thanks the financial support of the Spanish Ministry of Science and Innovation to the project MAT2013-41099-R. DL and SS acknowledge the European Regional Development Fund in the IT4Innovations national supercomputing centre-Path to Exascale (Project number CZ.02.1.01/0.0/0.0/16_013/0001791) within the Operational Programme Research, Development and Education, and DL acknowledges also the project No. 17-27790S of Czech Science Foundations and Mobility grant No. 8×17046.

[1] L.I. Kosse, E.D. Politova, V.V. Chechkin, E.A. Myzgin, and Y.N. Medvedev, B.S., Venevtsevae, Izv Akad Nauk SSSR, Neorg Mater **18(11)**, 1879 (1982).

[2] L.I. Kosse, E.D. Politova, and Y.N. Venevtsev, Zhurnal Neorg. Khim. **28**, 1689 (1983).

[3] M. Herak, H. Berger, M. Prester, M. Miljak, I. Zivkovic, O. Milat, D. Drobac, S. Popovic, and O. Zaharko, J. Phys. Condens. Matter **17**, 7667 (2005).

[4] K.Y. Choi, P. Lemmens, E.S. Choi, and H. Berger, J. Phys. Condens. Matter **20**, 505214 (2008).

[5] M. Hudl, R. Mathieu, S.A. Ivanov, M. Weil, V. Carolus, T. Lottermoser, M. Fiebig, Y. Tokunaga, Y. Taguchi, Y. Tokura, and P. Nordblad, Phys. Rev. B **84**, 180404 (2011).

[6] S.A. Ivanov, P. Nordblad, R. Mathieu, R. Tellgren, C. Ritter, N. V Golubko, E.D. Politova, and M. Weil, Mater. Res. Bull. **46**, 1870 (2011).

[7] S.A. Ivanov, R. Tellgren, C. Ritter, P. Nordblad, R. Mathieu, G. Andre, N.V. Golubko, E.D. Politova, and M. Weil, Mater. Res. Bull. **47**, 63 (2012).

[8] R. Mathieu, S.A. Ivanov, P. Nordblad, and M. Weil, Eur. Phys. J. B **86**, 1 (2013).

[9] S.A. Ivanov, R. Mathieu, P. Nordblad, R. Tellgren, C. Ritter, E. Politova, G. Kaleva, A. Mosunov, S. Stefanovich, and M. Weil, Chem. Mater. **25**, 935 (2013).

[10] M.-R. Li, D. Walker, M. Retuerto, T. Sarkar, J. Hadermann, P.W. Stephens, M. Croft, A. Ignatov, C.P. Grams, J. Hemberger, I. Nowik, P.S. Halasyamani, T.T. Tran, S. Mukherjee, T.S. Dasgupta, and M. Greenblatt, Angew. Chemie Int. Ed. **52**, 8406 (2013).

[11] M.-R. Li, M. Retuerto, D. Walker, T. Sarkar, P.W. Stephens, S. Mukherjee, T.S. Dasgupta, J.P. Hodges, M. Croft, C.P. Grams, J. Hemberger, J. Sánchez-Benítez, A. Huq, F.O. Saouma, J.I. Jang, and M. Greenblatt, Angew. Chemie Int. Ed. **53**, 10774 (2014).

[12] Y.S. Oh, S. Artyukhin, J.J. Yang, V. Zapf, J.W. Kim, D. Vanderbilt, and S.-W. Cheong, Nat Commun **5**, 3201 (2014).

[13] J.W. Kim, S. Artyukhin, E.D. Mun, M. Jaime, N. Harrison, A. Hansen, J.J. Yang, Y.S. Oh, D. Vanderbilt, V.S. Zapf, and S.-W. Cheong, Phys. Rev. Lett. **115**, 137201 (2015).

[14] X. Wang, F.-T. Huang, J. Yang, Y.S. Oh, and S.-W. Cheong, APL Mater. **3**, 76105 (2015).

[15] S. Skiadopoulou, F. Borodavka, C. Kadlec, F. Kadlec, M. Retuerto, Z. Deng, M. Greenblatt, and S.

Kamba, Phys. Rev. B **95**, 184435 (2017).
[16] M.-R. Li, M. Croft, P.W. Stephens, M. Ye, D. Vanderbilt, M. Retuerto, Z. Deng, C.P. Grams, J. Hemberger, J. Hadermann, W.-M. Li, C.-Q. Jin, F.O. Saouma, J.I. Jang, H. Akamatsu, V. Gopalan, D. Walker, and M. Greenblatt, Adv. Mater. **27**, 2177 (2015).
[17] G. Bayer, Zeit. Krist. **124**, 131 (1967).
[18] H.G. Burckhardt, C. Platte, and M. Trömel, Acta Crystallogr. Sect. B Struct. Crystallogr. Cryst. Chem. **38**, 2450 (1982).
[19] J.A. Baglio and S. Natansohn, J. Appl. Crystallogr. **2**, 252 (1969).
[20] R. Becker, M. Johnsson, and H. Berger, Acta Crystallogr. Sect. C Cryst. Struct. Commun. **62**, i67 (2006).
[21] A. Hostachy and J. Coing-Boyat, C. R. Acad. Sci. **267**, 1425 (1968).
[22] H.M. Rietveld and IUCr, J. Appl. Crystallogr. **2**, 65 (1969).
[23] J. Rodríguez-Carvajal and Juan, Phys. B Condens. Matter **192**, 55 (1993).
[24] F. Gervais, in *Chap. 7 High-Temperature Infrared Reflectivity Spectrosc. by Scanning Interf. Vol. 8 Infrared Millim. Waves*, edited by K.J. Button (Academic, New York, 1983), p. 279.
[25] M. Tyunina, A. Dejneka, D. Rytz, I. Gregora, F. Borodavka, M. Vondracek, and J. Honolka, J. Phys. Condens. Matter **26**, 125901 (2014).
[26] G. Kresse and J. Furthmüller, Phys. Rev. B **54**, 11169 (1996).
[27] J.P. Perdew, K. Burke, and M. Ernzerhof, Phys. Rev. Lett. **77**, 3865 (1996).
[28] S.L. Dudarev, G.A. Botton, S.Y. Savrasov, C.J. Humphreys, and A.P. Sutton, Phys. Rev. B **57**, 1505 (1998).
[29] *Supplemental Information* (n.d.).
[30] R. Becker and H. Berger, Acta Crystallogr. Sect. E **62**, 222 (2006).
[31] I. Živković, K. Prša, O. Zaharko, and H. Berger, J. Phys. Condens. Matter **22**, 56002 (2010).
[32] S.A. Ivanov, P. Nordblad, R. Mathieu, R. Tellgren, C. Ritter, N.V. Golubko, E.D. Politova, and M. Weil, Mater. Res. Bull. **46**, 1870 (2011).
[33] L. Zhao, Z. Hu, C.-Y. Kuo, T.-W. Pi, M.-K. Wu, L.H. Tjeng, and A.C. Komarek, Phys. Status Solidi - Rapid Res. Lett. **9**, 730 (2015).
[34] S.A. Ivanov, C. Ritter, P. Nordblad, R. Tellgren, M. Weil, V. Carolus, T. Lottermoser, M. Fiebig, and R. Mathieu, J. Phys. D. Appl. Phys. **50**, 85001 (2017).
[35] Y. Tokura, S. Seki, and N. Nagaosa, Reports Prog. Phys. **77**, 76501 (2014).
[36] M.O. Yokosuk, S. Artyukhin, A. Al-Wahish, X. Wang, J. Yang, Z. Li, S.-W. Cheong, D. Vanderbilt, and J.L. Musfeldt, Phys. Rev. B **92**, 144305 (2015).
[37] G. Blasse and W. Hordijk, J. Solid State Chem. **5**, 395 (1972).
[38] P. Lunkenheimer, S. Krohns, S. Riegg, S.G. Ebbinghaus, A. Reller, and A. Loidl, Eur. Phys. J. Spec. Top. **180**, 61 (2009).
[39] A. Shuvaev, V. Dziom, A. Pimenov, M. Schiebl, A.A. Mukhin, A.C. Komarek, T. Finger, M. Braden, and A. Pimenov, Phys. Rev. Lett. **111**, 227201 (2013).